IEEE Access
Multidisciplinary | Rapid Review | Open Access Journal

Received May 7, 2020, accepted May 27, 2020, date of publication June 17, 2020, date of current version July 3, 2020.

Digital Object Identifier 10.1109/ACCESS.2020.3002992

Numerical Method for Horizontal and Vertical Spatial Resolutions of Seismic Acquisition Geometries in Complex 3D Media

WEI WEI[1,3], LI-YUN FU[2,4], JUN SU[1,3], GUOZHANG LIU[1,3], AND WEIJIA SUN[1,3]

[1]Key Laboratory of Petroleum Resource Research, Institute of Geology and Geophysics, Chinese Academy of Sciences, Beijing 100029, China
[2]Laboratory for Marine Mineral Resources, Qingdao National Laboratory for Marine Science and Technology, Qingdao 266071, China
[3]Innovation Academy for Earth Science, Chinese Academy of Sciences, Beijing 100029, China
[4]Key Laboratory of Deep Oil and Gas, China University of Petroleum (East China), Qingdao 266580, China

Corresponding author: Li-Yun Fu (lfu@upc.edu.cn)

This work was supported in part by the National Key Research and Development Program of China under Grant 2017YFB0202903, in part by the National Natural Science Foundation of China under Grant 41720104006 and Grant 41821002, and in part by the Strategic Priority Research Program of the Chinese Academy of Sciences under Grant XDA14010303.

ABSTRACT Spatial sampling, finite bandwidth, and overlying-strata shielding are three key issues to affect the spatial resolution of seismic imaging for deep targets. Some factors have a great impact on the horizontal resolution, whereas others influence the vertical resolution. How to quantify these effects remains controversial for complex media. Most previous studies on seismic acquisition geometries focus on the horizontal resolution for layered media but neglecting to measure the vertical resolution especially in complex media. Conventional criteria for vertical resolution are based on the theory of geometric seismology with the assumption of a simple medium. As a practical alternative for resolution estimation in complex media, numerical methods with wavefield extrapolation for focal-beam analysis can provide comprehensive insight into the combined effect of acquisition geometries, bandlimited frequencies, and complex media on the horizontal and vertical spatial resolutions of acquisition geometries. We incorporate some classic criteria into the focal-beam numerical analysis to measure the spatial resolutions. Four parameters are used to quantify the performance of acquisition geometries. The horizontal (vertical) resolution is defined as the main-lobe width of a focal beam along the horizontal (vertical) direction, whereas the square root of the peak-to-total ratio of energies is referred to as the horizontal (vertical) sharpness. These parameters describe the horizontal and vertical spatial resolution and sharpness to image the target. Numerical examples with typical acquisition geometries demonstrate the performance of numerical resolution analyses in complex media.

INDEX TERMS Seismic imaging, spatial resolutions, spatial sampling, acquisition geometry.

I. INTRODUCTION

Spatial sampling characterization of seismic acquisition geometries is a rapidly growing area of research because of its impact on seismic imaging. Prior resolution analyses of an acquisition geometry to predict the quality of acquired datasets can optimize the design of acquisition parameters before the implementation of seismic acquisition. However, there are still controversies about how to measure the effect of spatial sampling (e.g., sparse and un-uniform) on the performance of seismic imaging in complex media. Most previous studies on seismic acquisition geometries focus on the horizontal resolution in layered media [1]–[4]. Classic criteria for temporal vertical resolution [5] are modified from geometrical optics with the assumption of a simple medium. In practice, spatial sampling, finite bandwidth, and overlying-strata shielding have a significant influence on both the horizontal and vertical spatial resolutions of seismic imaging for deep targets. In this paper, numerical methods with wavefield extrapolation for focal-beam analysis are modified to investigate the combined effect of acquisition geometries, band-limited frequencies, and complex media on both the horizontal and vertical resolutions.

Quantification of the vertical resolution of acquisition geometries and associated influences have not yet been clarified especially in complex media. Traditional studies on the

The associate editor coordinating the review of this manuscript and approving it for publication was Yongqiang Zhao.

vertical resolution are mainly based on the minimum layer thickness that can be distinguished on seismic data composed of seismic waves vertically reflected by subsurface reflectors. The widely used methods for temporal vertical resolution are based on the Rayleigh, Ricker, and Widess criteria [6], [7]. These classic criteria have been extensively studied relevant to the limit of vertical and lateral resolutions [8]–[11], discuss the horizontal resolution limit [12]–[15] of migrated images in a homogeneous medium based on a Rayleigh-like zero-crossing criterion. Lee *et al.* [16] apply the classic criteria to resolution analyses for marine seismic acquisition. These classic criteria, however, only consider the case of a simple homogeneous or layered medium, leading to the analytical expression for normal-incidence responses.

Current industry techniques for seismic survey design do not directly target the imaging of complex structures. We need an effective tool to quantitatively measure image resolutions for seismic survey design in complex media. The imaging-driven design of seismic surveys must invoke the extrapolation of surface acquisition geometries to deep targets with complex geologic models. Ray-based techniques have been proposed for this purpose with imaging resolution analyses to evaluate the performance of acquisition geometries. Based on the Born approximation to scattered acoustic waves, Gibson and Tzimeas [17] extend the Beylkin's equation [2] to reconstruct the scattering image of a target point for the resolution analysis of a given geometry. The mapping are done by simple ray-tracing for the traveltimes and amplitudes from the source to target point and back to receivers. Gelius *et al.* [18] analyze the imaging resolution function of Born and Kirchhoff scattering models for the distorted and blurred effects because of a limited aperture and bandlimited signals. Lecomte [19] employs the ray-based approach to calculate the point-spread function (PSF) of point scatterers to identify the effect of various factors on the resolution of prestack depth migrations (PSDM). Despite finite accuracies without considering the frequency dependence and other wave phenomena, these approximation methods provide a simple yet effective tool to predict the spatial resolution of acquisition geometries for seismic imaging.

Wavefield extrapolation methods have been widely used for resolution analyses of both acquisition and imaging systems, which can be classified into two categories. For the first, the wave-equation extrapolation of wavefields from sources and receivers to subsurface targets establishes directional energy fluxes by a local plane-wave analysis at a target [20]. The resulting local energy matrices can be used to quantify the target illumination conditions. The local incident and scattered plane waves at the target for both sources and receivers can be used to calculate the PSF of point scatters [21], which can also be formulated based on the local angle domain decomposition of Green's functions [22]. The scattering PSF or local illumination matrices, however, only enable resolution/illumination analyses, rather than directly calculating the horizontal and vertical resolutions of seismic imaging. In addition, the wavefield extrapolation for both sources and receivers is computationally intensive, especially for 3D cases. The second category of wave-equation-based resolution analyses results from the focal beam theory [23], which can assess the spatial sampling for sources and receivers separately. In this paper, we modify the focal-beam resolution analysis to circumvent the problems involved with the first category.

Focal-beam analysis [24] can provide quantitative insight into the combined influence of acquisition geometries and subsurface structures on the resolution. The theory of focal-beam analysis in a homogeneous medium [25] has been extended to complex media [26] with a fast multi-frequency focal-beam analysis [27] used to investigate the effect of acquisition geometries on the horizontal resolution in complex 3D media [28]. Recent researches extend the focal-beam analysis to account for surface waves [29] and surface/internal multiples [30], [31]. Most the studies of focal-beam analysis address the horizontal resolution of acquisition geometries for seismic imaging. Although some simple examples of focal-beam analysis on the vertical resolution are presented [25], [26], quantitative studies on this issue are neglected as a whole, especially in complex media.

Following the studies on the horizontal resolution of acquisition geometries [28], [32], we incorporate classic resolution criteria into the multifrequency focal-beam method with an attempt to measure both the horizontal and vertical resolutions of acquisition geometries for seismic imaging in complex media. Unlike the aforementioned conventional wavefield extrapolation from sources (forward) and receivers (backward) to subsurface targets, we modify the focal beaming of wavefields by a more efficient way, that is, we mainly concern the upward continuation of wavefields from a deep target to the surface, significantly reducing the computational cost of high-density and wide-aperture seismic acquisitions. We formulate the spatial resolution function of multifrequency focal beams in complex 3D media. Four critical parameters calculated by the focal-beam analysis are used to quantify the horizontal and vertical resolutions (HR and VR) and their corresponding sharpness (HS and VS) in the depth domain for a given acquisition geometry. Based on the classic resolution criteria, the HR is defined as the horizontal main-lobe width determined at the 35%-amplitude points [33] of a focal-beam horizontal profile, with its HS as the square root of the ratio of the peak energy to the total energy of the horizontal profile. Similarly, the VR is measured as the distance between two inflection points determined by the second derivative of a focal-beam vertical profile. The corresponding VS is computed as the square root of the ratio of the peak energy to the total energy of the vertical profile.

We validate the proposed focal-beam resolution analysis by analytical methods for a simple medium. With several velocity models (including the 3D SEG/EAGE salt model), we investigate the effect of coverage deficiencies, detector-line lengths, and overlying high-velocity anomalies on the resolution of acquisition geometries. Case studies with

3D seismic data from an oil field in China demonstrate the utility of the proposed survey design tool. Prior HR, VR, HS, and VS analyses of an acquisition geometry will help to improve the design of acquisition parameters for seismic imaging.

II. HORIZONTAL AND VERTICAL SPATIAL-RESOLUTION MATRICES OF FOCAL BEAMS

The focal-beam analysis originates from seismic migration by the double focusing concept [1], [23], which can be explained by the WRW model [34]. For primary reflections, each frequency component $\mathbf{P}(z_0, z_0)$ of wavefields for pairing detectors and sources of a stationary acquisition geometry at the surface can be depicted as:

$$\mathbf{P}(z_0, z_0) = \mathbf{D}(z_0) \left[\sum_{m=1}^{M} \begin{matrix} \mathbf{W}(z_0, z_m)\, \mathbf{R}(z_m, z_m) \\ *\boldsymbol{W}(z_m, z_0) \end{matrix} \right] \mathbf{S}(z_0), \quad (1)$$

where, z_0 is the surface depth, and z_m is the depth of the m$^{\text{th}}$ reflection layer ($1 \le m \le M$) with M being the number of reflection layers. $\mathbf{D}(z_0)$ and $\mathbf{S}(z_0)$ represent the detector and source matrices, respectively. $\mathbf{W}(z_0, z_m)$ is a one-way propagator, which depicts upward wave propagation from depth z_m to z_0. $\mathbf{R}(z_m, z_m)$ is the reflectivity matrix at depth z_m, $\mathbf{W}(z_m, z_0)$ is a one-way propagator, which depicts downward wave propagation from depth z_0 to z_m, and * denotes matrix multiplications.

In the matrices above, each column and row indicate a lateral location of detectors and sources, respectively. The lateral coordinates (x, y) and the frequency ω are ignored for convenience. Only considering the reflection from a depth level z_m, equation (1) can be simplified as follows:

$$\mathbf{P}(z_0, z_0) = \mathbf{D}(z_0)\, \mathbf{W}(z_0, z_m)\, \mathbf{R}(z_m, z_m)\, \mathbf{W}(z_m, z_0)\, \mathbf{S}(z_0). \quad (2)$$

If the reflectivity is angle-independent, the total reflectivity matrix $\mathbf{R}(z_m, z_m)$ is a diagonal matrix as a sum of individual reflectivity matrices at gridpoints as follows:

$$\mathbf{R}(z_m, z_m) = \sum_k \delta_k \mathbf{R}(z_m, z_m), \quad (3)$$

where, k indicates the lateral location (x_k, y_k).$\delta_k \mathbf{R}(z_m, z_m)$ is the angle-independent reflectivity matrix including only one nonzero element at the gridpoint (x_k, y_k, z_m). It can be written as a matrix multiplication of a column vector and a row vector as follows:

$$\delta_k \mathbf{R}(z_m, z_m) = \mathbf{i}_k(z_m, z_m)\, \mathbf{i}_k^{\dagger}(z_m, z_m), \quad (4)$$

where $\mathbf{i}_k$ is a unit column vector that includes only one nonzero element at the gridpoint (x_k, y_k, z_m) and the dagger symbol ($\dagger$) denotes a row vector. According to the superposition principle of waves, $\mathbf{P}(z_0, z_0)$ can also be depicted as a sum of all gridpoint responses, as follows:

$$\mathbf{P}(z_0, z_0) = \sum_k \delta_k \mathbf{P}(z_0, z_0), \quad (5)$$

where $\delta_k \mathbf{P}(z_0, z_0)$ represents the seismic response of the gridpoint (x_k, y_k, z_m) with the detectors and sources at the surface, which can be written as,

$$\delta_k \mathbf{P}(z_0, z_0) = \mathbf{D}(z_0)\, \mathbf{W}(z_0, z_m)\, \delta_k \mathbf{R}(z_m, z_m) *\boldsymbol{W}(z_m, z_0)\, \mathbf{S}(z_0). \quad (6)$$

To evaluate the reflectivity at the target depth z_m, we need to extrapolate the gridpoint response $\delta_k \mathbf{P}(z_0, z_0)$ to the target depth z_m. This process is equivalent to prestack depth migration, which can be achieved by applying additional focusing operators $\mathbf{F}(z_m, z_0)$ and $\mathbf{F}(z_0, z_m)$ at both detector and source sides:

$$\begin{aligned} \delta_k \mathbf{P}(z_m, z_m) &= [\mathbf{F}(z_m, z_0)\, \mathbf{D}(z_0)\, \mathbf{W}(z_0, z_m)]\, \delta_k \mathbf{R}(z_m, z_m) \\ &\quad * [\mathbf{W}(z_m, z_0)\, \mathbf{S}(z_0)\, \mathbf{F}(z_0, z_m)] \\ &= \mathbf{d}_k(z_m, z_m)\, \mathbf{s}_k^{\dagger}(z_m, z_m), \end{aligned} \quad (7)$$

where $\delta_k \mathbf{P}(z_m, z_m)$ represents the double-focusing matrix. $\mathbf{d}_k(z_m, z_m)$ and $\mathbf{s}_k^{\dagger}(z_m, z_m)$ represent the focal-detector (a column vector) and focal-source (a row vector) beams for the gridpoint at (x_k, y_k, z_m), respectively. These beams can be defined as follows:

$$\begin{aligned} \mathbf{d}_k(z_m, z_m) &= \mathbf{F}(z_m, z_0)\, \mathbf{D}(z_0)\, \mathbf{W}(z_0, z_m)\, \mathbf{i}_k(z_m, z_m) \\ &= \mathbf{F}(z_m, z_0)\, \mathbf{D}(z_0)\, \mathbf{w}_k(z_0, z_m), \end{aligned} \quad (8)$$

and

$$\begin{aligned} \mathbf{s}_k^{\dagger}(z_m, z_m) &= \mathbf{i}_k^{\dagger}(z_m, z_m)\, \mathbf{W}(z_m, z_0)\, \mathbf{S}(z_0)\, \mathbf{F}(z_0, z_m) \\ &= \mathbf{w}_k^{\dagger}(z_m, z_0)\, \mathbf{S}(z_0)\, \mathbf{F}(z_0, z_m), \end{aligned} \quad (9)$$

where $\mathbf{w}_k(z_0, z_m)$ and $\mathbf{w}_k^{\dagger}(z_m, z_0)$ mean one-way propagation from a target point at the gridpoint (x_k, y_k, z_m) to detectors and sources, respectively.

In the double-focusing matrix $\delta_k \mathbf{P}(z_m, z_m)$, all the diagonal elements generate the resolution function $\delta_k \mathbf{p}(z_m, z_m)$, which can be calculated by an element-by-element multiplication of the focal-detector and the focal-source beams, as follows:

$$\delta_k \mathbf{p}(z_m, z_m) = \mathbf{d}_k(z_m, z_m) \otimes \mathbf{s}_k^{\dagger}(z_m, z_m), \quad (10)$$

where $\otimes$ denotes element-by-element multiplications. Ideally by making use of the perfect focusing operators $\mathbf{F}(z_m, z_0)$ and $\mathbf{F}(z_0, z_m)$, the wavefield energy can converge to the target point at the location (x_k, y_k, z_m), i.e., $\delta_k \mathbf{p}(z_m, z_m) = \mathbf{i}_k(z_m, z_m)$, which means the evaluated reflectivity equals to the real reflectivity after migration.

By applying the focusing operators $\mathbf{F}(z_n, z_0)$ and $\mathbf{F}(z_0, z_n)$ to a different level of focused depths $z_n (z_n \neq z_m)$ in (8) and (9), the resolution function can be expressed as:

$$\delta_k \mathbf{p}(z_n, z_n) = \mathbf{d}_k(z_n, z_m) \otimes \mathbf{s}_k^{\dagger}(z_m, z_n), \quad (11)$$

where $\mathbf{d}_k(z_n, z_m)$ and $\mathbf{s}_k^{\dagger}(z_m, z_n)$ represent the focal-detector and focal-source beams, respectively, from the target point (x_k, y_k, z_m) to the focused depth level z_n. They can be written as,

$$\mathbf{d}_k(z_n, z_m) = \mathbf{F}(z_n, z_0)\, \mathbf{D}(z_0)\, \boldsymbol{w}_k(z_0, z_m), \quad (12)$$

and

$$\mathbf{s}_k^{\dagger}(z_m, z_n) = \mathbf{w}_k^{\dagger}(z_m, z_0)\,\mathbf{S}(z_0)\,\mathbf{F}(z_0, z_n). \tag{13}$$

Ideally, $\delta_k\mathbf{p}(z_n, z_m) = \mathbf{o}(z_n, z_m)$ is a zero column vector, which means no wavefield energy leaks into the non-target depth levels in migration. Combining the resolution vectors at all the depths $(z_1, z_2, \ldots, z_m, \ldots, z_N)$ $(z_1 < z_m < z_N)$, we obtain a 3D spatial resolution matrix,

$$\delta_k\mathbf{B}(z_m) = \begin{bmatrix} \delta_k\mathbf{p}(z_1, z_1), \delta_k\mathbf{p}(z_2, z_2), \ldots, \\ \delta_k\mathbf{p}(z_m, z_m), \ldots, \delta_k\mathbf{p}(z_N, z_N) \end{bmatrix}^{\mathrm{T}}, \tag{14}$$

where the superscript T represents the matrix transposition. In the matrix $\delta_k\mathbf{B}(z_m)$, the column and row correspond to the depth z_n and horizontal position $k(x, y)$, respectively. It indicates that $\delta_k\mathbf{B}(z_m)$ is a function of the 3D spatial coordinates x, y, and z. It contains both the horizontal and vertical spatial-resolution functions. The ideal 3D spatial-resolution matrix can be expressed as follows,

$$\delta_k\mathbf{B}(z_m) = \begin{bmatrix} \mathbf{o}(z_1, z_1), \mathbf{o}(z_2, z_2), \ldots, \\ \mathbf{i}_k(z_m, z_m), \ldots, \mathbf{o}(z_N, z_N) \end{bmatrix}^{\mathrm{T}} = \mathbf{I}_k(z_m), \tag{15}$$

where $\mathbf{I}_k(z_m)$ contains only one nonzero element at (x_k, y_k, z_m). However, because actual acquisition geometries do not always satisfy the perfect focusing, $\delta_k\mathbf{B}(z_m) \neq \mathbf{I}_k(z_m)$. This offers an opportunity to evaluate the imaging performance of acquisition geometries using (14). By taking $y \equiv y_k$ or $x \equiv x_k$, $\delta_k\mathbf{B}(z_m)$ is reduced to its submatrices, $\delta_x\mathbf{B}(z_m)$ or $\delta_y\mathbf{B}(z_m)$, which represent a vertical slice at $y \equiv y_m$ or $x \equiv x_m$ of the full 3D spatial-resolution matrix. In addition, $\delta_k\mathbf{B}(z_m)$ can be extended to the non-stationary configuration of acquisition geometries by summing over all the templates,

$$\delta_k\mathbf{B}(z_m) = \sum_l \delta_k\mathbf{B}^{[l]}(z_m), \tag{16}$$

where superscript l is the template index. Note that only the focal beam of primary waves is discussed above with multiple reflections being ignored. To consider the effect of multiple reflections on the spatial resolution, the primary-wavefield focal beam can be extended to a full-wavefield focal beam that can include multiple waves in the manner of iterative modeling [30]. The full-wavefield focal beam can be used to analyze the nonlinear effect of complex media (e.g., high-velocity anomalies) on the horizontal and vertical resolutions, which will be discussed in the example section.

We then propose an alternative implementation for focal-beam analyses. We mainly consider the upward extrapolation of wavefields from the points around the target to the surface, significantly improving the computation efficiency especially for wide-aperture and high-density acquisition geometries. By ignoring the nonlinear factors, e.g., the effect of multiple reflections, the focusing operator $\mathbf{F}$ can be approximated as $\mathbf{F} = \mathbf{W}^{-1} \approx \mathbf{W}^{\mathrm{H}}$, where the superscript H represents the complex conjugate operation. Based on the reciprocity

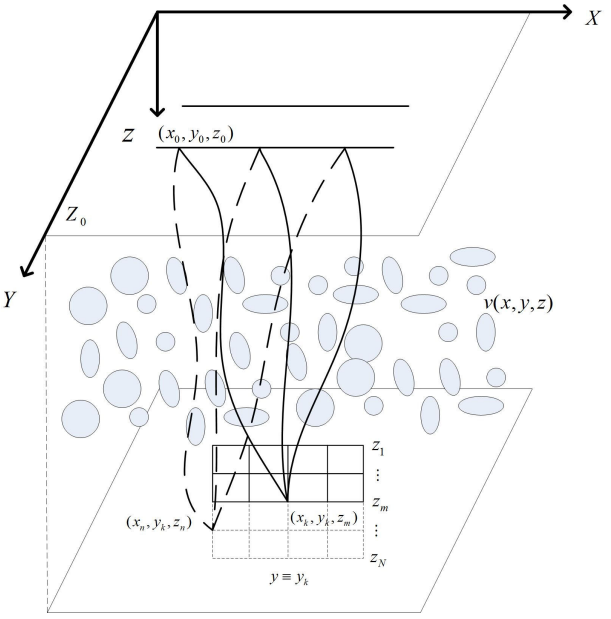

FIGURE 1. Schematic of resolution matrix computation. Wavefields are extrapolated from the target at (x_k, y_k, z_m) (solid line) and its adjacent grid points at (x_k, y_k, z_n) (dash lines), through heterogeneous media $v(x, y, z)$, to the surface sources and detectors at z_0, yielding the focal-source and focal-detector beams, respectively. The resolution matrix of acquisition geometry at the target can be estimated by multiplying the focal-source and focal-detector beams.

theorem [35], the focal-source beam obtained by (13) can be represented as,

$$\begin{aligned} \mathbf{s}_k^{\dagger}(z_m, z_n) &= \boldsymbol{w}_k^{\dagger}(z_m, z_0)\,\mathbf{S}(z_0)\,\mathbf{F}(z_0, z_n) \\ &= [\mathbf{F}(z_n, z_0)\,\mathbf{S}(z_0)\,\mathbf{w}_k(z_0, z_m)]^{\mathrm{T}} \\ &\approx \left[[\mathbf{W}(z_0, z_n)]^{\mathrm{H}}\,\mathbf{S}(z_0)\,\mathbf{w}_k(z_0, z_m)\right]^{\mathrm{T}}. \end{aligned} \tag{17}$$

Combining (17) and (12), the focal-detector and focal-source beams can be written as,

$$\mathbf{d}_k(z_n, z_n) \approx [\mathbf{W}(z_0, z_n)]^{\mathrm{H}}\,\mathbf{D}(z_0)\,\mathbf{w}_k(z_0, z_m), \tag{18}$$

and

$$\mathbf{s}_k^{\dagger}(z_m, z_n) \approx \left[[\mathbf{W}(z_0, z_n)]^{\mathrm{H}}\,\mathbf{S}(z_0)\,\mathbf{w}_k(z_0, z_m)\right]^{\mathrm{T}}. \tag{19}$$

Combining (11), (14), (18), and (19) yields a new implementation for the resolution matrix $\delta_k\mathbf{B}(z_m)$. Because we only use the upward extrapolation (forward) instead of using both the upward and downward extrapolations, the resulting computational cost depends mainly on the number of z_n and $k(x, y)$, rather than numerous parameters of an acquisition geometry, (especially, the inline and crossline rolling numbers). Therefore, the focal-beam implementation described by (18) and (19) can be expected to be more efficient for wide-aperture and high-density acquisitions than the conventional focal-beam implementation that involves both upward and downward extrapolations in complex media [26]. As shown in Figure 1, to estimate the horizontal and vertical resolutions at the target, we set some gridpoints around the

target, which are used as the sources for upward extrapolation of wavefields. Therefore, the number of these grid-points and associated modeling operations mainly affect the computational cost of implementing (14). Note that the primary-wavefield focal beam is considered during the implementation.

To reduce the computational cost further, we calculate the submatrix of $\delta_k \mathbf{B}(z_m)$ only, i.e., the $\delta_x \mathbf{B}(z_m)(y \equiv y_m)$ or $\delta_y \mathbf{B}(z_m)(x \equiv x_m)$ to obtain a vertical slice in the full 3D spatial-resolution matrix. Computation of the resolution matrix $\delta_x \mathbf{B}(z_m)$ consists of the following steps (see Figure 1),

(1) Select a target point at (x_k, y_k, z_m) located at depth z_m.

(2) Simulate forward propagation from the target point to the surface located at depth z_0 to obtain the wavefield $\mathbf{w}_k(z_0, z_m)$ and apply the acquisition geometry to select traces corresponding to source and receiver matrices $\mathbf{D}(z_0)$ and $\mathbf{S}(z_0)$.

(3) Define a 3D mesh around the target point. Note that there are some conditions on choosing the mesh range and spacing in every direction to ensure the accuracy of continued quantitative analysis of resolutions and sharpness, which will be discussed in the next sections.

(4) Simulate individually forward propagation from each point in the 3D mesh to the surface located at depth z_0 to obtain the propagator $\mathbf{W}(z_0, z_n)$ and apply the acquisition geometry to select traces corresponding to source and receiver matrices $\mathbf{D}(z_0)$ and $\mathbf{S}(z_0)$.

(5) Calculate the focal-detector beams by multiplying the wavefield emitted from the target point and the conjugates of the wavefields emitted from the grids around the target point according to (18).

(6) Calculate the focal-source beams by multiplying the wavefield emitted from the target point and the conjugates of the wavefields emitted from the mesh points around the target point according to (19).

(7) Substitute the focal-source and focal-detector beams into (11) and (14) to obtain the resolution function.

(8) Repeat steps (1) to (7) to obtain the resolution functions for different frequencies, and sum all the frequency components to obtain the multifrequency result.

(9) Sum beams for each template rolling to obtain the result of the non-stationary geometry.

In our focal-beam analysis, the wavefield extrapolation is implemented from the deepest layer to the shallow. The computational cost required for the multifrequency focal-beam analysis described above depends heavily on the method used for wavefield extrapolation. To achieve an acceptable trade-off between numerical accuracies and computational costs for given computer resources, we extrapolate wavefields through a thick slab by a degenerate Fourier operator [36], [37] and then interpolate wavefields for individual small layers inside the thick slab by a Born-Kirchhoff interpolation operator [38], [39]. The Fourier extrapolation technique with thick-slab extrapolation plus thin-slab interpolation can significantly enhance the efficiency of 3D multifrequency focal-beam analyses in complex media. We can improve the accuracy of focal-beam analyses by reducing the depth-step size for wavefield extrapolation and computing more single-frequency beams for interpolation but at the cost of computational efficiency.

III. COMBINATION OF FOCAL BEAMS AND CLASSIC CRITERIA FOR RESOLUTION ANALYSES

A. HORIZONTAL/VERTICAL RESOLUTION AND SHARPNESS

We first take an example to demonstrate the resolution analysis in homogeneous and heterogeneous media, respectively. The velocity of the homogeneous model is 4 km/s. The heterogeneous model has a dimension of 3 km (x) × 3 km (y) × 3 km (z) at a grid interval of 10 m, with $v_{\min} = 3.8$ km/s and $v_{\max} = 5.15$ km/s. The velocity gradients with respect to x-, y-, and z-axis are 2 s^{-1}, 1.5 s^{-1}, and 1 s^{-1}, respectively. The acquisition geometry includes one source and 11 detector lines with a 200 m spacing and each line containing 11 detectors with a 200 m interval. The focal-beam analysis for the target point at (1 km, 1 km, 1 km) is computed using a zero-phase Ricker wavelet with a peak frequency of 25 Hz. The bandwidth ranges from 1 Hz to 75 Hz with an interval of 1 Hz.

In an ideal case, the resulting resolution function converges to a point at the target location, as shown in Figure 2a. However, in practice, as shown in Figure 2b, the resolution function of focal beams always has a wider distribution with obvious sidelobe noises even in a homogeneous medium because of bandlimited frequencies, finite recording apertures, and discrete spatial samplings. For heterogeneous media, the effect of lateral velocity variations on focal beams further reduces the peak-to-total ratio by increasing sidelobe noises (see Figure 2c).

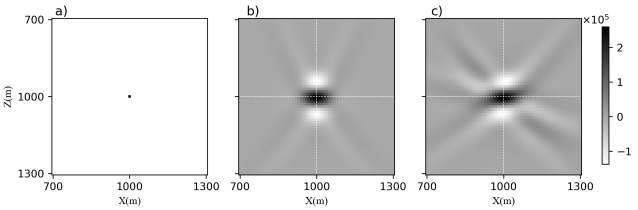

FIGURE 2. Comparison of resolution functions (a) for the ideal case, (b) in a homogeneous medium with a constant velocity of 4 km/s, and (c) in a heterogeneous model with varying velocities.

From the viewpoint of focused array theory of Kirchhoff summation, Safar [33] illustrates that two-point diffractors are resolved for the width of array responses at the 35%-amplitude points. Schoenberger [8] defines the vertical resolution by the peak-to-sidelobe ratio between the central-peak and sidelobe amplitudes. Koefoed [9] demonstrates that the seismic vertical resolution is influenced by three factors: the central-lobe width, the sidelobe ratio or peak-to-trough ratio, and the amplitude of side-tail oscillation. Kallweit and Wood [10] define the vertical temporal resolution in that two wavelets can be resolved when their spacing is greater than or equal to the separation between the

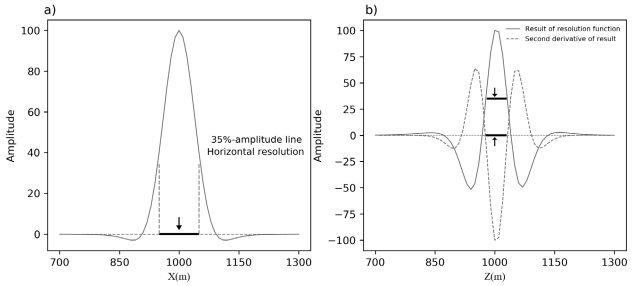

FIGURE 3. The horizontal (a) and vertical (b) profiles (solid line) extracted from Figure 2b along the horizontal (at z = 1 km) and vertical (at x = 1 km) directions, respectively. The derivative (dotted line) of the vertical profile helps to determine two vertical inflection points. The resolution parameters (HR and VR) and sharpness parameters (HS and VS) can be calculated from these profiles in the spatial domain.

wavelet's inflection points (referring to the Ricker limit [6]). The inflection points can be determined by the second derivative of the wavelet function. Based on the same physical implication, these traditional formulas can also be applied to describe the horizontal and vertical spatial resolutions of acquisition geometries.

Figure 3 shows the horizontal and vertical profiles (solid line) extracted from Figure 2b along the horizontal (at $z = 1$ km) and vertical (at $x = 1$ km) directions, respectively. Based on these profiles, we demonstrate how to calculate the two resolution parameters (HR and VR) and two sharpness parameters (HS and VS) in the spatial domain. The HR is defined as the horizontal main-lobe width, as marked by a thick solid line in Figure 3a and determined at the 35%-amplitude points [33] from the maximum amplitude. Similar to Widess [40], the HS can be calculated as the square root of the ratio of the peak energy to the total energy of the horizontal profile. Similarly, the VR is measured as the distance between two vertical inflection points, as marked by a thick solid line in Figure 3b. The vertical inflection points are determined by taking the second derivative (dotted line in the figure) of vertical profile to be zero. The VS is computed as the square root of the ratio of the peak energy to the total energy of the vertical profile. These characteristic parameters quantify the horizontal and vertical resolutions and their sharpness of an acquisition geometry for seismic imaging at the target.

For clarity, we rewrite the resolution function $\delta_k \mathbf{B}(z_m)$ as $b(x, y, z)$. The horizontal resolution is defined as

$$HR = |x_{i1} - x_{i2}|, \tag{20}$$

where $i1 \neq i2$. The amplitude of $b(x_{i1}, y_k, z_m)$ and $b(x_{i2}, y_k, z_m)$ equals to 35 percent of the maximum amplitude $b(x_k, y_k, z_m)$ in the resolution function at the target point, i.e., $b(x_{i1}, y_k, z_m) = b(x_{i2}, y_k, z_m) = 0.35 * b(x_k, y_k, z_m)$. The vertical resolution is defined by

$$VR = \left|z_{j1} - z_{j2}\right|, \tag{21}$$

where $j1 \neq j2$. The second derivative of $b(x_k, y_k, z_{j1})$ and $b(x_k, y_k, z_{j2})$ equal to zero, i.e., $\frac{\partial^2 b(x_k, y_k, z_{j1})}{\partial z^2} = \frac{\partial^2 b(x_k, y_k, z_{j2})}{\partial z^2} = 0$. Note that the values of HR and VR may change with x- and z-directional mesh spacings around the target. For more accurate estimation of HR and VR, the z-directional spacing should be less than half the wavelength, whereas the x-directional spacing should be less than or equal to the bin size.

The sharpness is generally defined as the peak-to-total ratio of a resolution function. It is inversely proportional to migration noises and has a significant impact on the signal-to-noise ratio [40] of an acquisition geometry for seismic imaging at the target. The sharpness of the spatial resolution function $b(x, y, z)$ is obtained by

$$S = \sqrt{\frac{[b(x_k, y_k, z_m)]^2}{\sum\limits_{x,y,z} [b(x, \mathrm{y}, \mathrm{z})]^2}}. \tag{22}$$

The vertical sharpness (**VS**) can be obtained from a vertical slice ($b(x, y_k, \mathrm{z})$) in the full 3D spatial resolution matrix by

$$VS = \sqrt{\frac{[b(x_k, y_k, z_m)]^2}{\sum\limits_{x,z} [b(x, y_k, \mathrm{z})]^2}}. \tag{23}$$

Similarly, the horizontal sharpness (**HS**) can be obtained from a horizontal slice ($b(x, \mathrm{y}, z_k)$) by

$$HS = \sqrt{\frac{[b(x_k, y_k, z_m)]^2}{\sum\limits_{x,y} [b(x, \mathrm{y}, z_k)]^2}}. \tag{24}$$

Note that the HS and VS values may also change with x- and z-directional meshing spacing and range around the target. For the computational stability of HS and VS values, the meshing spacing should meet the needs of HR and VR calculation as previously mentioned, and the meshing range around the target should be large enough to ensure the wavefield amplitude reduced enough toward the border, less than 0.1% of the maximum amplitude.

B. BENCHMARK MODEL FOR VALIDATION

Comparisons of focal-beam analyses and classic resolution criteria are conducted for benchmark tests in a homogeneous medium. The homogeneous medium has a velocity of 3 km/s, with the target depth being 5 km. The horizontal and vertical sampling rates around the target area are 10 m and 2 m, respectively. The acquisition geometry includes 51 source- and detector-lines with a 20 m line interval. Each line contains 51 sources and detectors with a 20 m spacing. The focal-beam analysis is computed using a zero-phase Ricker wavelet with a peak frequency of 45 Hz. The geometry template is not rolled during the process of acquisition.

With the benchmark model, we compute resolution functions for various peak frequencies. The HR and VR as functions of frequency are extracted by the 35%-amplitude criterion [33] and the $1/e$-amplitude criterion [28], respectively. The results are shown in Figure 4, compared with the analytical HR estimates [13] and the analytical VR estimates by the Ricker criterion [10]. We see that the focal-beam

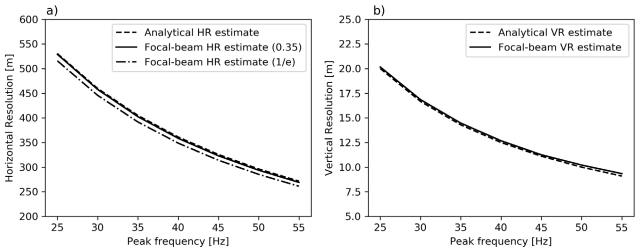

FIGURE 4. Comparison of the focal-beam numerical method and analytical estimations for horizontal (a) and vertical (b) resolutions versus frequency.

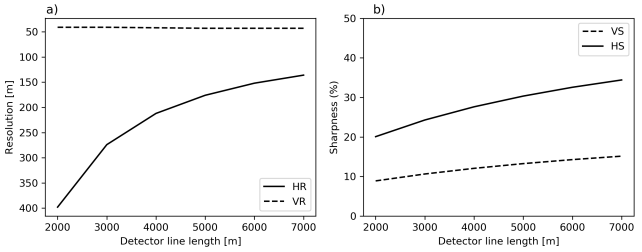

FIGURE 6. The horizontal/vertical resolutions (a) and sharpness (b) versus detector-line lengths, estimated by the focal-beam analysis in a homogeneous medium for a peak frequency of 25 Hz with other acquisition parameters unchanged.

numerical results agree well with the analytical estimates for all the frequencies. As is expected, both the HR and VR increase with increasing frequencies. The focal-beam HR by the $1/e$-amplitude criterion shows some minor departures from the analytical estimate because of $1/e \approx 0.368$ a little larger than 0.35, overestimating the horizontal resolution of acquisition geometries. The focusing process can be regarded as an alternative way of migration [23] with a wavelet stretch applied and affecting the imaging resolution [4]. The analytical estimation by classic resolution criteria ignores the influence of migration process. In this simple example with a homogeneous medium, there is less wavelet stretch in focal beams, leading to consistent resolution estimates with classic criteria.

IV. IMPACT OF KEY ACQUISITION FACTORS

A. DETECTOR-LINE LENGTHS

Focal-beam analyses are conducted for acquisition geometries with different detector-line lengths. These templates consist of 21 detector lines and 5 source lines both with a 50 m line spacing and a 50 m detector (source) interval, but having different detector-line lengths from 2 km, 3 km,..., to 7 km. The target is at depth of 5 km below the center of the spread. The focal-beam analysis for a 25 Hz Ricker wavelet is computed in a homogeneous medium with a constant velocity of 3.5 km/s. The horizontal and vertical sampling rates of resolution function are 10 m and 1 m, respectively. The resulting resolution functions with the detector-line length 2 km, 5 km, and 7 km are shown in Figure 5.

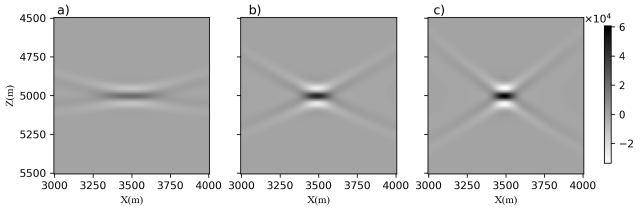

FIGURE 5. The resolution functions with the detector-line length 2 km (a), 5 km (b), and 7 km (c) for a peak frequency of 25 Hz with other acquisition parameters unchanged.

The resolution functions for all the detector-line lengths are computed and used to extract the HR, HS, VR, and VS, as shown in Figure 6 versus detector-line lengths. We see that the HR and HS significantly enhance with increasing detector-line lengths, but the VR and VS remain almost unchanged. The vertical resolution is essentially affected by the maximum wavenumber along the vertical direction [41]. Different detector-line lengths contribute varying horizontal wavenumbers and hence influence the horizontal resolution rather than the vertical resolution.

B. HIGH-VELOCITY ANOMALIES

Overlying high-velocity anomalies generally impact on the performance of surface acquisition geometries for imaging a deep target. For example, high-velocity salts often reduce the resolution beneath the salt structure [17]. However, the decreased resolution can be improved by increasing detector-line lengths as demonstrated in the previous section. This section uses focal-beam analyses to quantify the effect of high-velocity anomalies on the horizontal and vertical resolution properties of acquisition geometries.

As used in classic resolution analyses [10], [13], a simple 2.5D wedge model with gradual changes in thickness is used to demonstrate the difference between the focal-beam and classic resolution analyses. As shown in Figure 7 for the x/z-section, the 2.5D model containing a wedge has a dimension of 6 km (x) $\times$ 1.5 km (z) with the wedge ranging from 2 km to 6 km in the x-axis direction and from 0.5 km to 1 km in the z-axis direction. Velocities are 3 km/s in

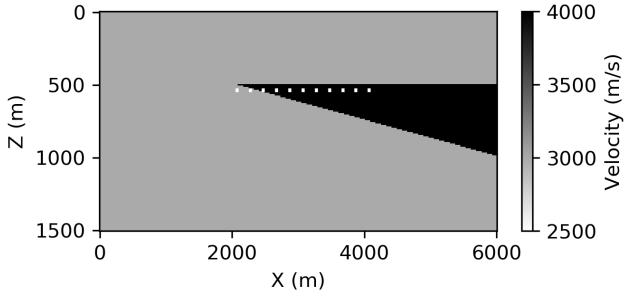

FIGURE 7. The x/z-section of a 2.5D wedge velocity model with the target points (white points) at (x = 2 km, 2.2 km, 2.4 km, . . . , 4 km, z = 0.55 km). Velocities are 3 km/s in the background and 4 km/s in the wedge, respectively. The focal-beam analysis for the target points is conducted using a Ricker wavelet of 25 Hz (peak frequency) with a bandwidth of 5 to 75 Hz.

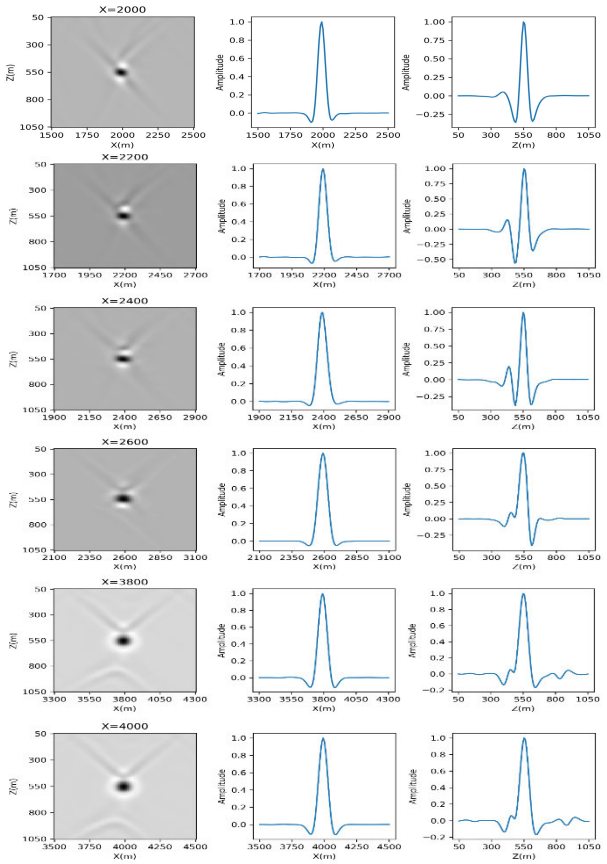

FIGURE 8. The resolution functions (left panel), target-crossing horizontal (middle panel) and vertical (right panel) profiles for the first four and last two target points at (x = 2 km, 2.2 km, 2.4 km, 2.6 km, 3.8 km, 4 km, z = 0.55 km).

the background and 4 km/s in the wedge, respectively. The full-wavefield focal-beam analyses for the target points at ($x = 2$ km, 2.2 km, 2.4 km, ..., 4 km, $z = 0.55$ km) are conducted using a Ricker wavelet of 25 Hz (peak frequency) with a bandwidth of 5 to 75 Hz. The 3D acquisition geometry consists of 61 detector lines with 3 km in length and 50 m for both line spacing and detector interval. There is a source located at the center of the spread. The spatial sampling rate is 10 m consistent with the model grid interval.

Strong lateral variations in velocity presented in the wedge model significantly change both the horizontal and vertical wavenumbers across the array of target points, which affects the horizontal and vertical resolution properties of acquisition geometries. The resulting focal beams and their target-crossing horizontal and vertical profiles are shown in Figure 8 for the first four and last two target points at ($x = 2$ km, 2.2 km, 2.4 km, 2.6 km, 3.8 km, 4 km, $z = 0.55$ km). We see that the shapes of both profiles with associated properties vary gradually from the first target point to the last. The strong nonlinear effect of complex waves occurs around the pinch-out of the wedge, including scattered waves by the external point and multiples by the top and bottom of the wedge. The thin-bed interference reduces gradually toward the right, particularly after the distinguishable thickness in the wedge model. Noted that the complex waves, as well as the thin-bed interference, obviously affect the extraction of HR, HS, VR, and VS.

The extracted HR, HS, VR, and VS for the target points are shown in Figure 9 versus their x-coordinates. These resolution curves are not quite smooth because of the interference by complex waves aforementioned. As expected from the lateral variations in velocity, both the horizontal/vertical resolution and sharpness have dramatic changes across the wedge. Lateral variations in both wedge thickness and velocity affect the horizontal/vertical wavenumbers of acquisition geometries. The resultant horizontal/vertical resolution properties shown in Figure 9 can be categorized into three situations in terms of the location of target points. (1) The target points with $x < 2.4$ km are located in the background medium and have rather high horizontal/vertical resolutions with few effects by complex waves. (2) The target points near the bottom interface (2.4 km) of the wedge have the strongest effect of complex waves and characterize abnormal horizontal/vertical resolutions. (3) The target points with $x > 2.4$ km are located in the high-velocity wedge and have rather low horizontal/vertical resolutions. For ease of comparison, the classic vertical resolution analysis is performed by a 25 Hz (peak frequency) and zero-phase Ricker wavelet, with the result marked by the black squares shown in Figure 9a.

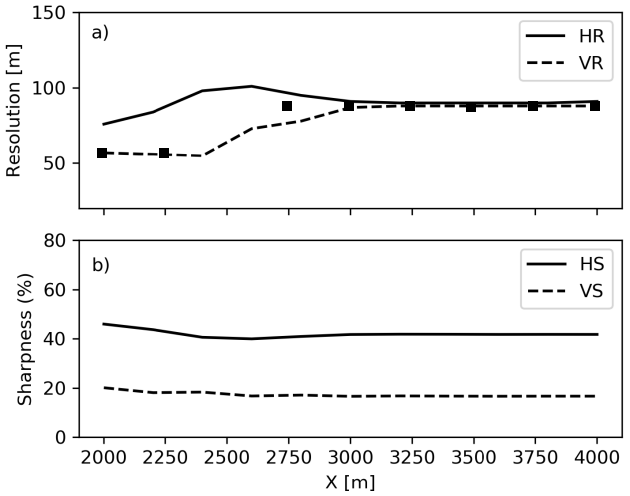

FIGURE 9. The horizontal/vertical resolutions (a) and sharpness (b) across the array of target points shown in Figure 8, estimated by the focal-beam analysis for a peak frequency of 25 Hz. The black squares represent the classical vertical resolutions.

C. COVERAGE DEFICIENCIES

Practical constraints to the implementation of acquisition geometries often cause coverage deficiencies because of obstacles such as lakes, rivers, and buildings. These coverage deficiencies, also referred as coverage holes, definitely destroy the quality of acquired data. Evaluation of data degradation has been extensively studied in terms of amplitude

losses and time shifts in the final migrated image compared to a reference model with full coverage [31], [42], [43]. In this paper, we address this issue by focal-beam resolution analyses.

As shown in Figure 10, the model with a dimension of 3 km (x) $\times$ 3 km (z) m contains several coverage holes with the size set as 0 km, 0.8 km, and 1.6 km, respectively. The acquisition geometry contains 31 source- and detector-lines with a 100 m line spacing, and each line containing 31 sources and detectors at a 100 m interval. The resolution function of acquisition geometries is computed for a homogeneous medium with a velocity of 4 km/s. The target point is located at (2 km, 1.5 km). A 25 Hz Ricker wavelet is used with a bandwidth ranging from 1 Hz to 75 Hz at an interval of 1 Hz. The geometry template is not rolled during the process of acquisition. The horizontal and vertical sampling rates are 10 m and 5 m, respectively. A coverage hole around the center of the spread is created by removing all the sources and detectors inside the square area.

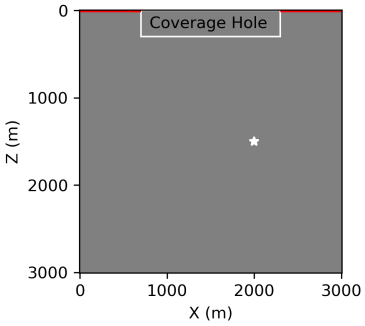

FIGURE 10. The model with a dimension of 3 km (x) × 3 km (z) and the target point at (2 km, 1.5 km) (marked by an asterisk) contains a coverage hole with the size set as 0 km, 0.8 km, and 1.6 km, respectively. The deficient coverage is created by removing all the sources and detectors within the hole.

As shown in Figure 11, the resolution functions with different hole sizes are calculated for the target point at (2 km, 1.5 km). As expected sensibly, the focusing effect becomes worse with increasing hole sizes. Both the horizontal/vertical resolution properties are affected by the deficient coverage of acquisition geometries. The main-lobe energy diverges gradually, associated with strong sidelobe perturbations that destroy the sharpness of acquisition geometries. We notice that the deficient coverage impacts the horizontal resolution and sharpness significantly more than the vertical resolution and sharpness because of few effects on the vertical wavenumber.

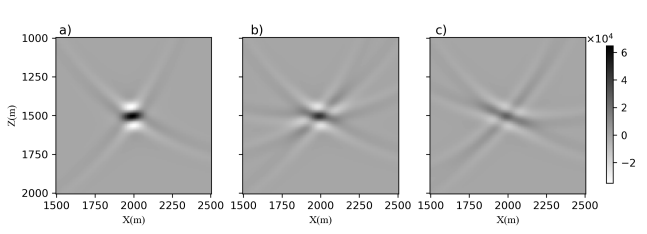

FIGURE 11. The resolution functions for the deficient coverages of 0 km, 0.8 km, and 1.6 km. The focal-beam analysis for the target point is conducted using a Ricker wavelet of 25 Hz (peak frequency) with a bandwidth of 5 to 75 Hz.

V. EXAMPLES

A. 3D SEG/EAGE SALT MODEL

We apply the focal-beam resolution analysis to the 3D SEG/EAGE salt model [44] as shown in Figure 12a. We set two different target points (see Figure 12b) located above and under the salt, respectively. The velocity model contains a complex subsalt structures with strong velocity contrasts and is often used as a good benchmark to test various imaging algorithms. We discretize the model by a grid interval of 10 m for both lateral and vertical directions. The acquisition geometry shown in Figure 12c contains 23 detector lines at 200 m spacing. Each line with 4.7 km in length contains 48 detectors at 100 m interval. The geometry template with two sources at 100 m interval is not rolled during the process of acquisition.

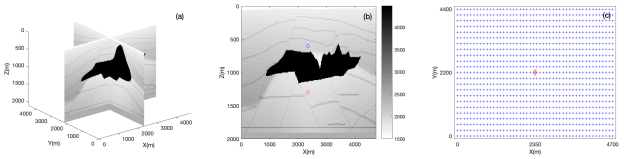

FIGURE 12. (a) The 3D SEG/EAGE salt model with a dimension of 4.75 km (x) × 4.5 km (y) × 2.09 km (z) at 10 m grid intervals for all directions, (b) Its 2D xz-section with two target points (red circle) at (2 km, 2.3 km, 0.6 km) and (2 km, 2.3 km, 1.3km), and (c) The acquisition template consisting of 23 detector lines at 200 m spacing and with each 4.7 km in length and containing 48 detectors (indicated by the cross +). Two sources with a 100 m interval are marked by an asterisk.

The focal-beam analysis is conducted using a Ricker wavelet of 25 Hz (peak frequency) with a bandwidth of 5 to 75 Hz. The spatial sampling rate is 10 m consistent with the grid interval of the model. The resulting resolution functions are shown in Figure 13 with the extracted resolution properties printed in the figure. As expected, the resolution function for the subsalt target becomes divergent seriously because of the distortion of subsalt wavefields, significantly impairing both the horizontal/vertical resolution and sharpness of acquisition geometries.

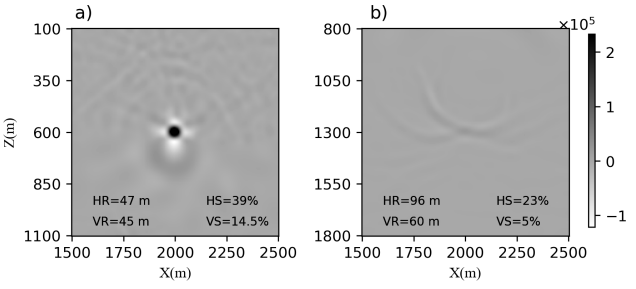

FIGURE 13. The resolution functions for the oversalt (a) and subsalt (b) targets with the extracted resolution properties marked in the figure.

B. CASE STUDY

In this section, we demonstrate an example of focal beam analysis applied to different acquisition geometries for an oilfield in China. As is shown in Figure 14, two orthogonal acquisition templates are exampled as Schemes I and II. Both of them contain 16 detector lines with 100 m spacing between lines and 4 km in length and three sources with 100 m source intervals. The detector intervals of Scheme I are 50 m, while Scheme II is a simplified version derived from Scheme I, with 100-m detector spacing. And the full folds (160) are same for the two acquisition geometries, where each geometry template is rolled during the acquisition three times transversely with each time crossline-rolling distance of 400 m, and 20 times longitudinally with an inline-rolling distance of 100 m.

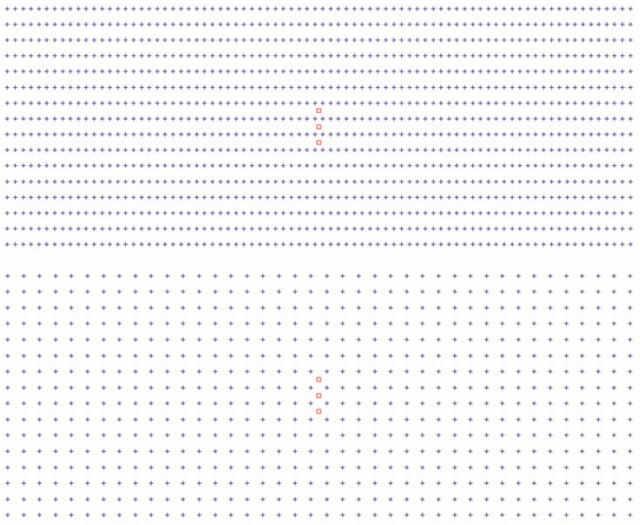

FIGURE 14. Two land survey acquisition templates of Scheme I (top panel) and II (lower panel). Both of them consist of 16 detector lines with 100 m spacing between lines and 4 km in length and 3 sources with 100 m source intervals. The intervals of detectors are 50 m and 100 m, respectively. The cross indicates detectors and the square represents sources.

We apply focal beam analysis to both schemes for a dominant frequency of 20 Hz with a frequency range of 10-35 Hz. The velocity model (see Figure 15), with a dimension of 12.5 km (x) × 5 km (y) × 5.2 km (z), contains several layers and some complex subsurface structures with velocities ranging from 5.2 km/s in the bottom layer to 2.1 km/s in the top layer. The model grid intervals are 10 m for vertical direction and 25 m for both lateral directions. The target point is located at the (3.125 km, 1.25 km, 2.3 km). We calculated separately every single frequency from 10 to 35 Hz with a spacing of 5 Hz and then added each focal beam to get the final result.

We apply the focal beam analysis to a homogeneous medium with the geometries schemes. The resulting VRs for both cases are 9.4 m, but with slightly different VSs of 23.0% (see Figure 16a) and 23.4% (see Figure 16b), respectively. In the heterogeneous medium, the resulting focal beams become disperse with larger VRs than that in the homogeneous medium. The estimated VRs for both cases are

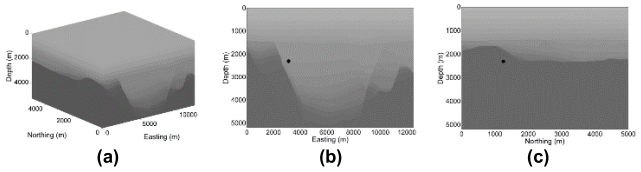

FIGURE 15. The 3D velocity model of an oilfield in China. The velocity model with a dimension of 12.5 km (x) × 5 km (y) × 5.2 km (z), contains some complex subsurface structures with velocity range from 5.2 km/s in the bottom layer to 2.1 km/s in the top layer. The model grid intervals are 10 m for vertical direction and 25 m for both lateral directions. The target point is located at the (3.125 km, 1.25 km, 2.3 km).

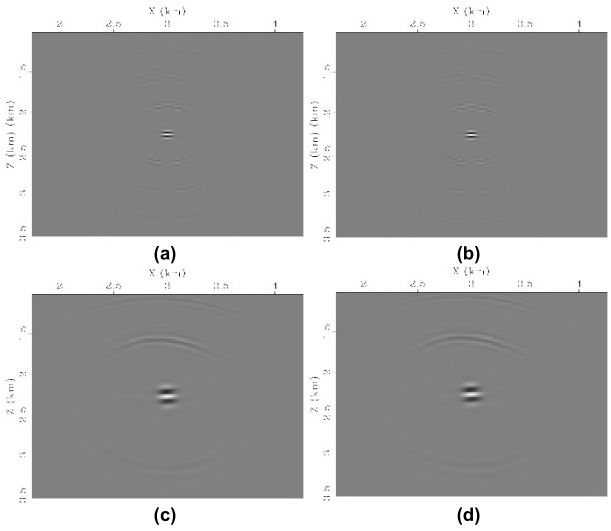

FIGURE 16. Focal beams of Scheme I (left) and Scheme II (right) for a homogeneous medium (top panel) and the velocity model (lower panel) shown in Figure 15 with the target point at (3.125 km, 1.25 km, 2.3 km).

24.4 m, with slightly different VSs of 12.3% (see Figure 16c) and 13.4% (see Figure 16d). For complex media, the effect of velocity variations will increase the VR and decrease the VS of acquisition geometry. The same VR values of two Schemes means similar vertical resolution for migration imaging in heterogeneous media. However, Scheme I with denser detectors has a lager value of VS than Scheme II, indicating more clarity in seismic imaging.

From the original real data which was gathered by implemented a 3D densely sampled seismic acquisition in an oilfield of China, we arrange seismic data according to Scheme I and II, respectively. And the seismic data is processed with the same parameters and procedure. The migration images for both Schemes at inline 830 are shown in Figure 17, and ''zoomed in'' sections from selected zones are also shown. We can see from the Figures that the two migration imaging sections are almost the same, but the profile of Scheme I has clearer continuous reflections and details, especially the small units like the faults and pinch-out, than the profile of Scheme II. In other words, Scheme I produces a higher S/N ratio with more clarity in imaging. And these seismic migration imaging comparisons agree with the previous focal beam analysis for Scheme I and II.

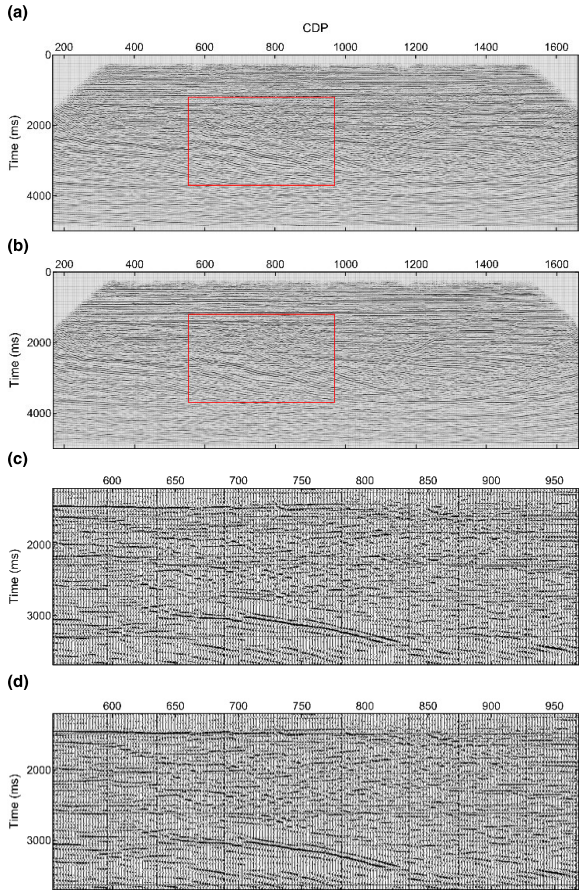

FIGURE 17. The seismic migration imaging profiles at inline 830 for Scheme I (a) and II (b) and their enlarged sections for Scheme I (c) and II (d).

VI. DISCUSSION AND CONCLUSION

The main purpose of our paper is to develop a method to quantify the imaging performance of acquisition geometries in complex media by combining the characteristics of conventional resolution criteria with the focal-beam analysis. The focal-beam results agree well with those by the classic-criterion estimation for a given acquisition geometry in a homogeneous medium with different peak frequencies. This method can also be extended to a full-wavefield resolution analysis to evaluate the nonlinear effects of the vertical and horizontal resolutions produced by complex media, e.g., high-velocity anomalies.

The effects of coverage holes and detector-line lengths on the imaging quality are assessed. With the increasing coverage hole sizes, the vertical resolution and sharpness computed by using vertical 3D resolution matrix slice slightly reduces, while the horizontal resolution and sharpness computed by only using resolution function profile along horizontal direction are significantly enhanced. The vertical resolution remains essentially unchanged when only the primaries are considered, whereas the horizontal resolution and sharpness reduce with increasing side lengths of high-velocity anomalies.

We apply the focal-beam method to a revised 3D SEG/EAGE salt model for a given acquisition geometry with two different target points and obtain different horizontal and vertical resolutions and sharpness. The combined effects of complex subsurface structures, velocity variations, and target depths impair the resolutions and sharpness of acquisition geometry. The prior analyses of acquisition geometries described by the resolutions and sharpness of focal beams can be helpful to indicate the performance of acquisition geometries for seismic imaging.

REFERENCES

[1] A. J. Berkhout, *Seismic Resolution: A Quantitative Analysis of Resolving Power of Acoustical Echo Techniques*. London, U.K.: Geophysical Press, 1984.
[2] G. Beylkin, "Imaging of discontinuities in the inverse scattering problem by inversion of a causal generalized radon transform," *J. Math. Phys.*, vol. 26, no. 1, pp. 99–108, Jan. 1985.
[3] T. A. Dickens and G. A. Winbow, "Spatial resolution of diffraction tomography," *J. Acoust. Soc. Amer.*, vol. 101, no. 1, pp. 77–86, Jan. 1997.
[4] S. A. Levin, "Resolution in seismic imaging: Is it all a matter of perspective?" *Geophysics*, vol. 63, no. 2, pp. 743–749, Mar. 1998.
[5] R. E. Sheriff, "Nomogram for Fresnel-zone calculation," *Geophysics*, vol. 45, no. 5, pp. 968–972, May 1980.
[6] N. Ricker, "Wavelet contraction, wavelet expansion, and the control of seismic resolution," *Geophysics*, vol. 18, no. 4, pp. 769–792, Oct. 1953.
[7] M. B. Widess, "How thin is a thin bed?" *Geophysics*, vol. 38, no. 6, pp. 1176–1180, Dec. 1973.
[8] M. Schoenberger, "Resolution comparison of minimum-phase and zero-phase signals," *Geophysics*, vol. 39, no. 6, pp. 826–833, Dec. 1974.
[9] O. Koefoed, "Aspects of vertical seismic resolution," *Geophys. Prospecting*, vol. 29, no. 1, pp. 21–30, Feb. 1981.
[10] R. S. Kallweit and L. C. Wood, "The limits of resolution of zero-phase wavelets," *Geophysics*, vol. 47, no. 7, pp. 1035–1046, Jul. 1982.
[11] S. Phadke and E. R. Kanasewich, "The resolution possible in imaging with diffracted seismic waves," *Geophys. Prospecting*, vol. 38, no. 8, pp. 913–931, May 1990.
[12] D. V. Seggern, "Spatial resolution of acoustic imaging with the Born approximation," *Geophysics*, vol. 56, no. 8, pp. 1185–1202, Aug. 1991.
[13] H. Chung and D. C. Lawton, "Amplitude responses of thin beds: Sinusoidal approximation versus ricker approximation," *Geophysics*, vol. 60, no. 1, pp. 223–230, Jan. 1995.
[14] J. Chen and G. T. Schuster, "Resolution limits of migrated images," *Geophysics*, vol. 64, no. 4, pp. 1046–1053, Jul. 1999.
[15] Y. Huang and G. T. Schuster, "Resolution limits for wave equation imaging," *J. Appl. Geophys.*, vol. 107, pp. 137–148, Aug. 2014.
[16] H.-Y. Lee, W. Kim, N.-H. Koo, K.-P. Park, D.-G. Yoo, D.-H. Kang, Y.-G. Kim, G.-S. Seo, and K.-D. Hwang, "Resolution analysis of shallow marine seismic data acquired using an airgun and an 8-channel streamer cable," *J. Appl. Geophys.*, vol. 105, pp. 203–212, Jun. 2014.
[17] R. L. Gibson and C. Tzimeas, "Quantitative measures of image resolution for seismic survey design," *Geophysics*, vol. 67, no. 6, pp. 1844–1852, Nov. 2002.
[18] L.-J. Gelius, I. Lecomte, and H. Tabti, "Analysis of the resolution function in seismic prestack depth imaging," *Geophys. Prospecting*, vol. 50, no. 5, pp. 505–515, Sep. 2002.
[19] I. Lecomte, "Resolution and illumination analyses in PSDM: A ray-based approach," *Lead. Edge*, vol. 27, no. 5, pp. 650–663, May 2008.
[20] X.-B. Xie, S. Jin, and R.-S. Wu, "Wave-equation-based seismic illumination analysis," *Geophysics*, vol. 71, no. 5, pp. S169–S177, Sep. 2006.
[21] R. Yan, H. Guan, X. B. Xie, and R. S. Wu, "Acquisition aperture correction in the angle domain toward true-reflection reverse time migration," *Geophysics*, vol. 79, no. 6, pp. S241–S250, Nov. 2014.
[22] R.-S. Wu and L. Chen, "Directional illumination analysis using beamlet decomposition and propagation," *Geophysics*, vol. 71, no. 4, pp. S147–S159, Jul. 2006.
[23] A. J. Berkhout, "Pushing the limits of seismic imaging, Part I: Prestack migration in terms of double dynamic focusing," *Geophysics*, vol. 62, no. 3, pp. 937–953, May 1997.
[24] A. J. Berkhout, L. OngKiehong, A. W. F. Volker, and G. Blacquière, "Comprehensive assessment of seismic acquisition geometries by focal beams—Part I: Theoretical considerations," *Geophysics*, vol. 66, no. 3, pp. 911–917, May 2001.

[25] A. W. F. Volker, G. Blacquière, A. J. Berkhout, and L. OngKiehong, "Comprehensive assessment of seismic acquisition geometries by focal beams—Part II: Practical aspects and examples," *Geophysics*, vol. 66, no. 3, pp. 918–931, May 2001.
[26] E. J. van Veldhuizen, G. Blacquière, and A. J. Berkhout, "Acquisition geometry analysis in complex 3D media," *Geophysics*, vol. 73, no. 5, pp. Q43–Q58, Sep. 2008.
[27] W. Wei, L.-Y. Fu, and G. Blacquière, "Fast multifrequency focal beam analysis for 3D seismic acquisition geometry," *Geophysics*, vol. 77, no. 2, pp. P11–P21, Mar. 2012.
[28] W. Wei and L.-Y. Fu, "On horizontal resolution for seismic acquisition geometries in complex 3D media," *J. Appl. Geophys.*, vol. 108, pp. 43–52, Sep. 2014.
[29] T. Ishiyama, G. Blacquière, D. J. Verschuur, and W. Mulder, "3D surface-wave estimation and separation using a closed-loop approach," *Geophys. Prospecting*, vol. 64, no. 6, pp. 1413–1427, Nov. 2016.
[30] A. Kumar, G. Blacquière, and E. Verschuur, "Extending illumination using all multiples: Application to 3D acquisition geometry analysis," *Geophys. Prospecting*, vol. 64, no. 3, pp. 622–641, May 2016.
[31] A. Kumar, G. Blacquière, M. W. Pedersen, and A. Goertz, "Full-wavefield marine survey design using all multiples," *Geophysics*, vol. 81, no. 3, pp. P1–P12, May 2016.
[32] J. Su, L.-Y. Fu, W. Wei, J. Hu, and W. Sun, "Focal beam analysis for 3D acquisition geometries in complex media with GPU implementation," *Comput. Geosci.*, vol. 118, pp. 39–51, Sep. 2018.
[33] M. H. Safar, "On the lateral resolution achieved by kirchhoff migration," *Geophysics*, vol. 50, no. 7, pp. 1091–1099, Jul. 1985.
[34] A. J. Berkhout, *Seismic Migration: Imaging of Acoustic Energy by Wave-field Extrapolation, A. Theoretical Aspects*. Amsterdam, The Netherlands: Elsevier, 1982.
[35] K. Wapenaar, "Reciprocity properties of one-way propagators," *Geophysics*, vol. 63, no. 5, pp. 1795–1798, Sep. 1998.
[36] L.-Y. Fu, "Comparison of different one-way propagators for wave forward propagation in heterogeneous crustal wave guides," *Bull. Seismol. Soc. Amer.*, vol. 96, no. 3, pp. 1091–1113, Jun. 2006.
[37] C. Tang, L.-Y. Fu, W. Pan, Q. Li, and J. Huang, "Optimized pseudo-Padé Fourier migrator in terms of propagation angles," *IEEE Access*, vol. 8, pp. 32054–32065, 2020.
[38] L. Fu, "Wavefield interpolation in the Fourier wavefield extrapolation," *Geophysics*, vol. 69, no. 1, pp. 257–264, Jan. 2004.
[39] G. X. Chen, L. Y. Fu, W. Wei, and W. Sun, "Wavefield interpolation in 3D large-step Fourier wavefield extrapolation," *Geophys. Prospecting*, vol. 66, no. 2, pp. 311–326, Mar. 2017.
[40] M. B. Widess, "Quantifying resolving power of seismic systems," *Geophysics*, vol. 48, no. 8, pp. 1687–1690, Aug. 1982.
[41] G. J. O. Vermeer, "Factors affecting spatial resolution," *Geophysics*, vol. 64, no. 3, pp. 942–953, May 1999.
[42] M. Brink, N. Jones, J. Doherty, V. Vinje, and R. Laurain, "Infill decisions using simulated migration amplitudes," in *Proc. SEG Tech. Program Expanded Abstr.*, Jan. 2004, pp. 57–60.
[43] A. Day and T. Rekdal, "Determining infill specifications based on geophysical criteria," in *Proc. SEG Tech. Program Expanded Abstr.*, Jan. 2005, pp. 30–35.
[44] F. Aminzadeh, N. Burkhard, J. Long, T. Kunz, and P. Duclos, "Three dimensional SEG/EAGE models–An Update," *Lead. Edge*, vol. 15, no. 2, pp. 131–134, Feb. 1996.
[45] J. Hoffmann, "Illumination, resolution, and image quality of PP- and PS-waves for survey planning," *Lead. Edge*, vol. 20, no. 9, pp. 1008–1014, Sep. 2001.

WEI WEI received the B.S. and M.S. degrees in geophysics from the China University of Geosciences, Wuhan, China, in 2003 and 2006, respectively, and the Ph.D. degree in geophysics from the Institute of Geology and Geophysics, Chinese Academy of Sciences, Beijing, China, in 2009.

From 2009 to 2014, he was a Postdoctoral Fellow in geophysics with the Institute of Geology and Geophysics, Chinese Academy of Sciences, where he has been an Associate Professor, since 2015. He was also a Visiting Researcher with the Delphi Research Consortium, Delft University of Technology, Delft, The Netherlands, in 2014 and 2017. His research interests include seismic wave modeling, seismic imaging, and seismic acquisition design.

LI-YUN FU received the B.S. degree in petroleum exploration from the Chengdu University of Technology, Chengdu, China, in 1985, and the M.S. and Ph.D. degrees in geophysics from the China University of Petroleum, Beijing, China, in 1992 and 1995, respectively.

From 1995 to 1997, he was a Postdoctoral Fellow of engineering mechanics with Tsinghua University. From 1997 to 1999, he was a Postdoctoral Fellow of tectonic structure with the University of California at Los Angeles (UCLA). From 1999 to 2004, he was a Research Scientist with the Commonwealth Scientific and Industrial Research Organization (CSIRO) and the Australian Resources Research Centre, and simultaneously, he was also a Visiting Professor with the College of Physics, Curtin University, Australia. From 2002 to 2003, he was a Visiting Researcher with the Institute of Geophysics and Planetary Physics (IGPP), UCLA. From 2004 to 2017, he was the Group Leader of seismology with the Institute of Geology and Geophysics, Chinese Academy of Sciences, Beijing. Since 2017, he has been a Professor with the School of Geosciences, China University of Petroleum (East China), Qingdao, China. He is currently a Professor with the Laboratory for Marine Mineral Resources, Qingdao National Laboratory for Marine Science and Technology, Qingdao. His research interests include regional seismic facies, crustal seismic wave propagation, seismic simulation, and imaging of complex geological structures.

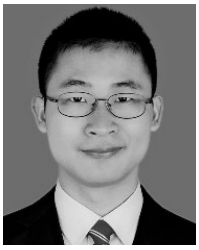

JUN SU received the B.S. and M.S. degrees in geophysics from the China University of Geosciences, Beijing, China, in 2012 and 2015, respectively, and the Ph.D. degree in geophysics from the Institute of Geology and Geophysics, Chinese Academy of Sciences, Beijing, in 2019.

His research interests include seismic data processing, seismic imaging, and seismic data acquisition.

GUOZHANG LIU received the B.S. degree in exploration technology and engineering from the Chengdu University of Technology, Chengdu, China, in 2016. He is currently pursuing the M.S. degree in geophysics with the Institute of Geology and Geophysics, Chinese Academy of Sciences, Beijing, China.

His research interests include seismic acquisition geometry design, seismic wavefield simulation, and image resolution analyses.

WEIJIA SUN received the Ph.D. degree in geophysics from the Institute of Geology and Geophysics, Chinese Academy of Sciences, Beijing, China, in 2010.

Since 2013, he has been with the Institute of Geology and Geophysics, Chinese Academy of Sciences, as an Associate Professor. He has solid research experiences of exploration geophysics in the past years. His primary research interests include deep lithospheric structures via newly developed seismic imaging techniques and planetary seismology.